Electrically Tunable Graphene Terahertz Isolator Assisted by Nonreciprocal Plasmon

Chen-Ran Xu(徐晨燃)[1,2*], Weiru Fan(范伟如)[1,2], Yanhao Tang(汤衍浩)[1,2], and Dawei Wang(王大伟)[1,2]

[1]*School of Physics, Zhejiang University, Hangzhou 310027, China*
[2]*Zhejiang Key Laboratory of Micro-Nano Quantum Chips and Quantum Control, Zhejiang University, Hangzhou 310027, China*

(Received 26 September 2024; accepted manuscript online 17 December 2024)

Nonreciprocal isolators enable unidirectional light propagation without back-reflection. Typical terahertz isolators require magnetic fields to break the time-reversal symmetry. Herein, we propose a nonmagnetic isolator in the terahertz range based on nonreciprocal graphene plasmons operated in a reflection configuration. The bias voltage generates a drift current in graphene, which breaks the time-reversal symmetry and induces nonreciprocal reflection. The isolator device exhibited a high isolation exceeding 20 dB with an insertion loss of less than 3 dB. Moreover, the bandwidth wit isolation exceeding 20 dB can be broadened five times to 1.7 THz by tuning the carrier density. The indexes, including the isolation, insertion loss and bandwidth of the isolator, show a strong dependence on the drift velocity and mobility of graphene, as well as the air-gap thickness. Our study shows great potential in the burgeoning terahertz technology, where nonmagnetic and electrically tunable isolators are still lacking.

DOI: 10.1088/0256-307X/42/1/014201 CSTR: 32039.14.0256-307X.42.1.014201

Terahertz (THz) science and technology have advanced rapidly over the past decade and extended into interdisciplinary areas, including wireless communications,[1–3] medical diagnostics,[4] imaging,[5] and sensing.[6] Although rich scientific and technological opportunities exist, the lack of efficient fundamental THz components, including THz sources, detectors, and basic functional devices hinders the development of THz technologies.[7] Specifically, an isolator is a fundamental nonreciprocal device to realize unidirectional propagation. These devices, which are analogous to optical diodes, play a significant role in protecting THz sources and suppressing multipath interference by cancelling back reflection.[8]

Traditional THz isolators based on the Faraday effect[9] and magneto-optical Kerr effect[10] are realized using magnetic-optical materials with polarization-converting properties. Various materials, such as semiconductors,[11,12] semimetals[13,14], and ferrofluid materials[15] have been proposed to realize THz isolators by generating the polarization rotation of THz light. Integrated on-chip terahertz isolators have also been demonstrated in systems including waveguides and resonators.[16] However, these devices require large magnetic fields to break the time-reversal symmetry to realize nonreciprocity, which unavoidably requires cumbersome equipment and hinders their application. Recently, ferrite THz isolators, containing permanent magnets, have been demonstrated to exhibit excellent properties of a large operational bandwidth at room temperature without the need for an external magnetic field; however, they are limited by large intrinsic losses.[9]

In the following section, we propose a nonmagnetic THz graphene isolator assisted by a nonreciprocal surface plasmon operating in the reflection configuration, i.e., a one-way THz mirror. A drift current is generated to break the time-reversal symmetry[17] and realize nonreciprocal reflection. The device exhibits a high isolation of 20 dB, a low insertion loss of less than 3 dB, and excellent electrical tunability.

Figure 1(a) shows a schematic of the proposed THz graphene isolator based on the Otto configuration. The structure was composed of a semi-cylindrical prism and a substrate with an air gap of several micrometers, which was used to excite the graphene surface plasmons.[18,19] The graphene mounted on the substrate was attached to two gold electrodes, which applied a bias voltage to generate a drift current to induce nonreciprocal reflection, that is, realizing a one-way mirror.

The angle-dependent reflection spectrum of the device was calculated in transverse magnetic mode using a transfer matrix. The conductivity of graphene in the long-wavelength limit can be described by the following form:[20,21]

$$\sigma = \frac{e^2 E_{\mathrm{F}}}{\pi\hbar^2}\frac{i}{\omega + i\tau^{-1}} + \frac{e^2}{4\hbar}\Big[\theta(\hbar\omega - 2E_{\mathrm{F}}) + \frac{i}{\pi}\log\Big|\frac{\hbar\omega - 2E_{\mathrm{F}}}{\hbar\omega + 2E_{\mathrm{F}}}\Big|\Big]. \quad (1)$$

Specifically, e denotes the electron charge, $\hbar$ denotes the Planck constant. Furthermore, $\theta(x)$ denotes the Heaviside

*Corresponding author. Email: crxu@zju.edu.cn
© 2025 Chinese Physical Society and IOP Publishing Ltd. All rights, including for text and data mining, AI training, and similar technologies, are reserved.

step function, where $\theta(x) = 1$ for $x \geq 0$ and $\theta(x) = 0$ for $x < 0$. Furthermore, τ represents the momentum relaxation time due to impurities or phonon-mediated scattering, which can be expressed as $\tau = \mu E_{\rm F}/ev_{\rm F}^2$.[21]. μ denotes the mobility of graphene charge carriers, whose values can reach 10^4–$10^6\,{\rm cm}^2/{\rm Vs}$.[22] Fermi energy $E_{\rm F}$ takes the form of $E_{\rm F} = \hbar v_{\rm F}\sqrt{\pi n}$, where n denotes the carrier density, which can be controlled by an applied gate voltage, and $v_{\rm F} = 10^6\,{\rm m/s}$ denotes the Fermi velocity of electrons. Under a drift current with drift velocity $v_{\rm d}$, the conductivity of graphene can be expressed as[23,24]

$$\sigma(v_{\rm d},\, k_x) = \frac{\omega}{\omega - v_{\rm d}k_x}\sigma_g(\omega - v_{\rm d}k_x), \tag{2}$$

where k_x denotes the wave-vector component along the drift direction, and $\sigma_{\rm g}$ denotes conductivity of graphene in the absence of drift current or magnetic bias. To excite the surface plasmons of graphene in the Otto configuration, a prism with a high permittivity is required to provide a large wave vector along x axis, which was chosen to be a TiO_2 ceramic with a permittivity of 100 in our model.[25] The refractive index of the substrate was 1.47.[26]

Figure 1(b) displays the reflection spectra as a function of incident angle θ for forward (positive angle) and backward (negative angle) incidence. The parameters here are $n = 1.5 \times 10^{12}\,{\rm cm}^{-2}$, $\mu = 5 \times 10^5\,{\rm cm}^2/{\rm Vs}$, $v_{\rm d} = v_{\rm F}/2$, and the air-gap thickness is set to be $1\,\mu{\rm m}$. The two curved strips of low reflection intensity displayed in dark color represent the nonreciprocal dispersion relationship of the graphene plasmons. As shown in Fig. 1(c), the reflection spectra at specific angles of $\pm 58.5°$ exhibit two separated dips at 1.17 THz and 1.38 THz, demonstrating the nonreciprocal reflection at these two incident frequencies. The main criteria for an excellent isolator include high isolation, low insertion loss, and broad bandwidth. For a negative incident angle, the isolation is defined as $R_{\rm backward} - R_{\rm forward}$, as shown in Fig. 1(d). The orange region of the positive isolation value denotes the effective bandwidth of the isolator for a negative incidence. The maximum isolation reached 35 dB at 1.38 THz, accompanied by a bandwidth of 0.022 (0.068) THz, with an isolation beyond 20 (10) dB. The case of a positive incident angle, marked by the blue line, shows similar isolation and bandwidth properties. Correspondingly, the insertion loss of isolator, which equals to 1-R, is shown in Fig. 1(e). At 1.38 THz, with maximum isolation, the insertion loss was as low as 1.2 dB. Moreover, the average insertion loss was 1.22 (1.19) dB for isolation beyond 20 (10) dB. The large isolation combined with the low insertion loss demonstrates the excellent performance of the designed non-magnetic THz isolator.

Next, we extend the analysis of isolation and insertion losses to the full range of incident angles, as shown in Figs. 2(a) and 2(b), respectively. The orange (blue) curved strip in Fig. 2(a) represents the region of high isolation at negative (positive) incident angles. Figure 2(b) shows the corresponding insertion loss, where the orange (blue) contour denotes the region with isolation beyond 10 dB at a negative incident angle. Inside the contour, the light color implies that the insertion loss is low (less than 2 dB), indicating high isolation and insertion loss available for a broad bandwidth by tuning the incident angle.

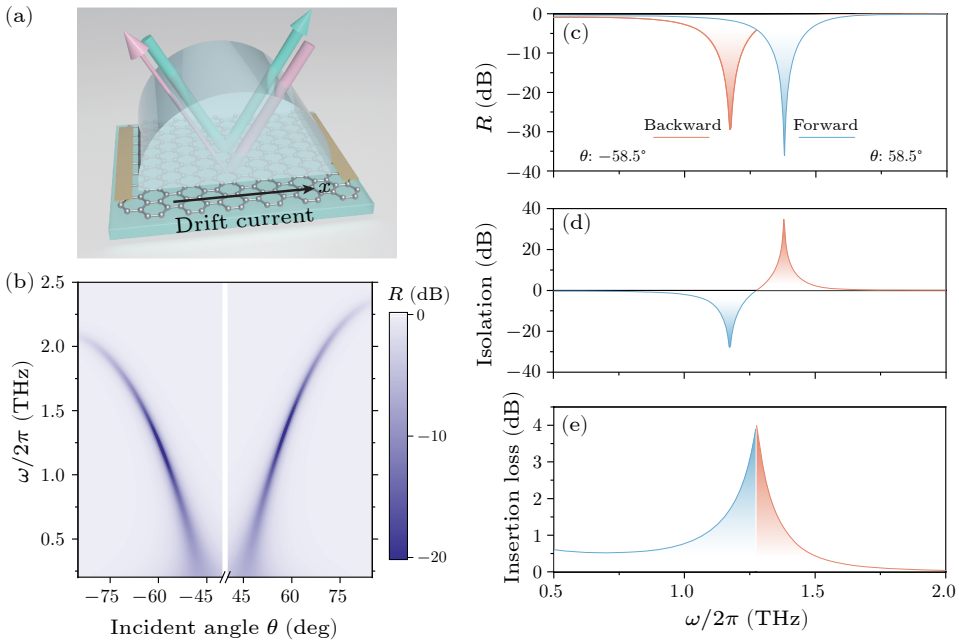

Fig. 1. (a) Schematic of the graphene THz isolator based on the Otto configuration. The bias voltage is applied to induce the drift current of graphene to break the reciprocity. (b) The reflection spectra as a function of incident angle in forward (right panel) and backward (left panel) incidence. (c) Reflection spectrum at $\theta = \pm 58.5°$. The corresponding isolation (d) and insertion loss (e).

We now analyze the isolation, insertion loss, and bandwidth in a comprehensive and quantitative manner to better characterize the isolator. For convenience, only cases with negative incidence were considered. Figure 2(c) shows the isolation at various incident angles. As the incident angle shifts from $-43°$ to $-89°$, the frequency of maximum isolation shifts from 0.3 to 2.3 THz, forming the envelop marked in the orange line with maximum isolation exceeding 40 dB. In this envelop, the frequency range with isolation beyond 20 dB is from 1.20 to 1.50 THz, corresponding to a bandwidth of 0.30 THz, realized by the tuning the incident angle. Moreover, for each incident angle, the bandwidth with isolation beyond 20 dB (10 dB) and the average insertion loss within this range are shown in Figs. 2(d) and 2(e), respectively, where x axis denotes the frequency of maximum isolation at this incident angle. Under the restriction of isolation beyond 10 dB, the bandwidth reaches 0.07 THz, combined with a low insertion loss of approximately 1.7 dB. In the case of an isolation exceeding 20 dB, the bandwidth decreases to 0.016 THz, along with an insertion loss of 1.2 dB. Consequently, the isolator can realize the nonreciprocal reflection with high isolation and low insertion loss for an available bandwidth of 0.3 THz by choosing the appropriate incident angle.

Inspired by the unique electrical properties of graphene, we examined the effect of the carrier density n of graphene on the performance of isolator devices. Specifically, n can be tuned by changing the Fermi level of graphene. Firstly, in Fig. 3(a), we show the isolation of the effective frequency range, i.e., the envelop in Fig. 2(c), at n varying from 0.8 to 2×10^{12} cm^{-2}. This indicates that the maximum isolation exceeds 35 dB for a wide range of n. Moreover, the isolation beyond 20 dB can be realized for a wide frequency range from 0.3 to 2.0 THz by sweeping n continuously, which broadens the effective bandwidth of the isolator by more than 5 times from the initial 0.3 THz to 1.7 THz. At each n, the bandwidth with isolation beyond 20 dB (10 dB) is also calculated and is shown with red (blue) dots in Fig. 3(b). As n increases from 0.8 to 2×10^{12}cm^{-2}, the bandwidth increases from 0.4 to 1.0 THz for isolation beyond 10 dB, while increases from 0.09 to 0.35 THz for isolation beyond 20 dB. Similar to the analysis in Figs. 2(d) and 2(e), the bandwidth with isolation beyond 10 dB and the relevant average insertion loss for each incident angle are shown in Figs. 3(c) and 3(d), respectively, where x axis represents the frequency of maximum isolation at the corresponding incident angle. The peak bandwidth decreases from 0.1 to 0.06 THz, whereas the median insertion loss decreases from 8 dB to 0.6 dB by more than one order of magnitude as n increases, indicating better performance of the isolator for a higher carrier density. The case of isolation beyond 20 dB exhibits a phenomenon similar to that shown in Figs. 3(e) and 3(f), where the bandwidth is three times smaller than that at 10 dB.

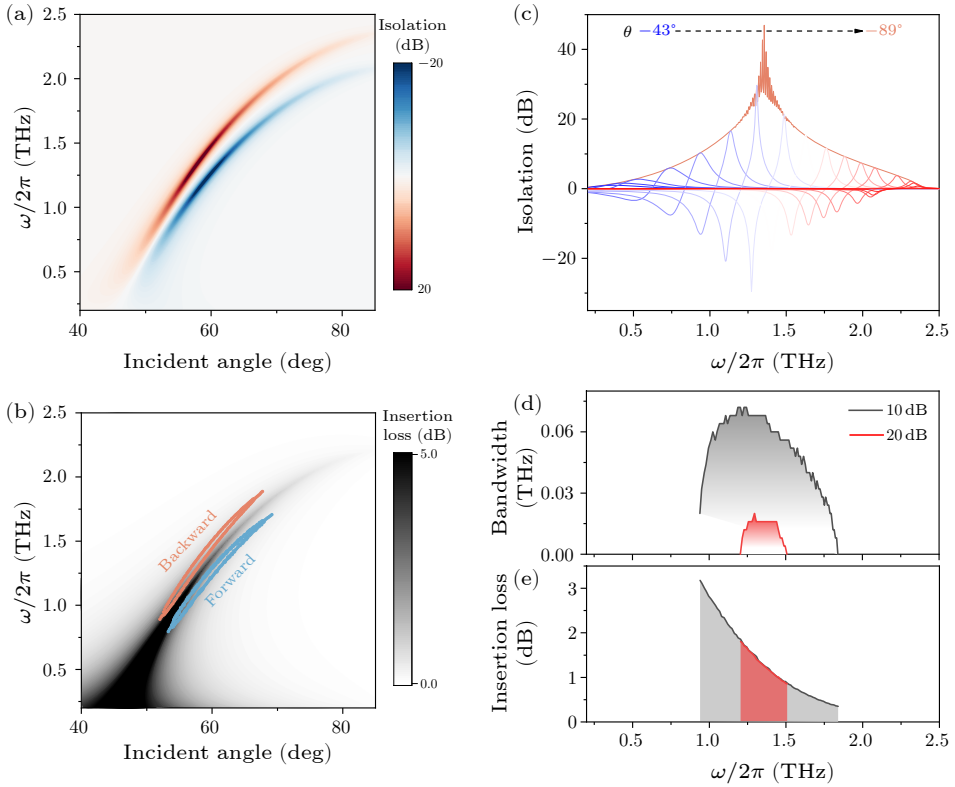

Fig. 2. (a, b) Isolation (a) and insertion loss (b) as functions of incident angle and frequency. (c) Isolation as a function of frequency for varying incident angles. The bandwidth with isolation beyond 20 (10) dB (d) and the average insertion loss within this range (e) for varying incident angles. The horizontal axis denotes the frequency of maximum isolation at the corresponding incident angle.

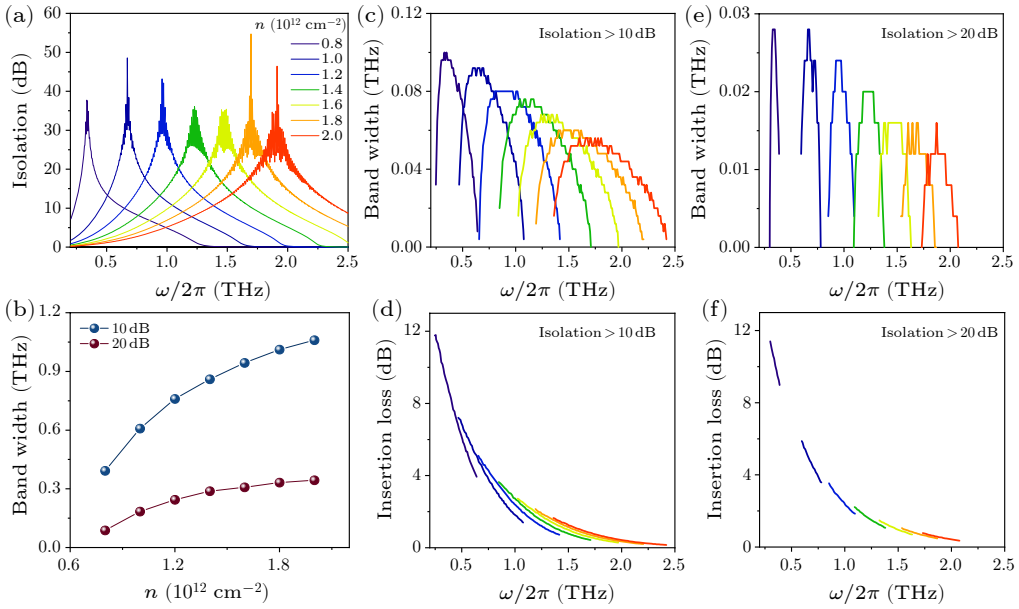

Fig. 3. Carrier density n dependent nonreciprocal reflection. (a) Isolation of the effective frequency range for varying n. (b) The bandwidth of each isolation curve of (a) under restriction of isolation exceeding 10 and 20 dB for varying n. For each incident angle, the bandwidth with isolation exceeding 10 dB (c) and average insertion loss within this range (d), where x axis denotes the frequency of maximum isolation at the corresponding incident angle. (e), (f) Furthermore, the case for isolation beyond 20 dB is the same.

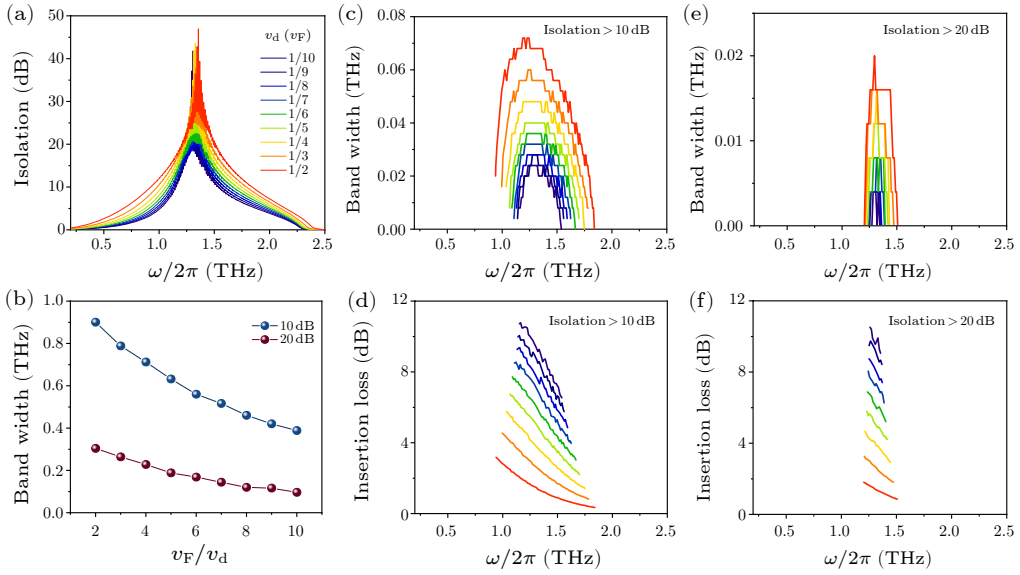

Fig. 4. Drift-velocity v_d dependent nonreciprocal reflection. (a) Isolation of the full frequency range for varying v_d. (b) The bandwidth of each isolation curve of (a) under restriction of isolation beyond 10 and 20 dB as a function of v_d. For each incident angle, the bandwidth with isolation beyond 10 dB (c) and the average insertion loss (d). (e), (f) The same case for isolation beyond 20 dB.

Given the nonreciprocity of the device arises from the drift current, the effect of the drift velocity v_d on the isolator device was also explored. The drift velocity can be controlled by varying the bias voltage applied to the gold electrodes, as shown in Fig. 1(a). Similar to the previous analysis of the carrier density, Figure 4(a) shows the isolation of the effective frequency range when $v_d$varies from $v_F/10$ to $v_F/2$, where the maximum isolation exceeds 40 dB for a wide range of v_d. Additionally, the bandwidth with isolations beyond 10 and 20 dB decrease by half as v_d decreases from $v_F/2$ to $v_F/10$, as shown in Fig. 4(b). For each incident angle, the bandwidth with an isolation greater than 10 dB and the corresponding average insertion losses are shown in Figs. 4(c) and 4(d), respectively. The peak bandwidth decreases from 0.07 to 0.02 THz, while the median insertion loss increases from 1.3 dB to 9 dB as v_d decreases from $v_F/2$ to $v_F/10$. For isolations beyond 20 dB, the bandwidth and insertion loss have similar properties, as shown in Figs. 4(e) and 4(f), where the bandwidth is three times smaller than that at 10 dB. The aforementioned results indicate that the isolator exhibits excellent performance with high isolation and low insertion loss un-

der a large drift velocity.

In summary, we proposed an electrically tunable nonmagnetic THz graphene isolator assisted by a nonreciprocal plasmon in the Otto configuration. The drift current induced by the electrical bias generates a nonreciprocal dispersion relationship of the plasmon, and thereby, induces nonreciprocal reflection. The isolator device shows high isolation beyond 20 dB with an insertion loss of less than 3 dB, which is available for a 0.3 THz bandwidth achieved by tuning the incident angles. Moreover, the isolator device exhibited electrical tunability owing to the outstanding properties of graphene, where the bandwidth of isolation beyond 20 dB can be broadened five times to 1.7 THz by tuning the carrier density. Additionally, the isolator exhibited excellent performance at a large drift velocity owing to its prominent non-reciprocity. The nonreciprocity of the isolator also depends on the mobility of graphene and air-gap thickness (see Supplementary Information). Considering the millimeter wavelength of the THz beam and oblique incident condition, the required size of the high-quality graphene sheet is on the millimeter scale. Fortunately, a technique for large-area exfoliation of graphene has been developed and millimeter-scale high-quality graphene can be fabricated, increasing the feasibility of our proposal.[27] Our results shed light on the THz technology and applications for which nonmagnetic and electrically tunable terahertz isolators are lacking.

Acknowledgements. Supported by the National Natural Science Foundation of China (Grant Nos. 11934011 and 12274365), National Key R&D Program of China (Grant Nos. 2022YFA1402400 and 2022YFA1400043), Zhejiang Provincial Natural Science Foundation of China (Grant No. LR24A040001), and Open project of Key Laboratory of Artificial Structures and Quantum Control (Ministry of Education) of Shanghai Jiao Tong University.

References

[1] Nagatsuma T, Ducournau G, and Renaud C C 2016 *Nat. Photon.* **10** 371
[2] Nagatsuma T 2011 *IEICE Electron. Express* **8** 1127
[3] Song H J and Nagatsuma T 2011 *IEEE Trans. Terahertz Sci. Technol.* **1** 256
[4] Zaytsev K I, Dolganova I N, Chernomyrdin N V, Katyba G M, Gavdush A A, Cherkasova O P, Komandin G A, Shchedrina M A, Khodan A N, Ponomarev D S, Reshetov I V, Karasik V E, Skorobogatiy M, Kurlov V N, and Tuchin V V 2020 *J. Opt.* **22** 013001
[5] Uerboukha H I G and Allappan K A N **10** 843
[6] Dhillon S S, Vitiello M S, Linfield E H, Davies A G, Hoffmann M C, Booske J, Paoloni C, Gensch M, Weightman P, Williams G P, Castro-Camus E, Cumming D R S, Simoens F, Escorcia-Carranza I, Grant J, Lucyszyn S, Kuwata-Gonokami M, Konishi K, Koch M, Schmuttenmaer C A, Cocker T L, Huber R, Markelz A G, Taylor Z D, Wallace V P, Axel Zeitler J, Sibik J, Korter T M, Ellison B, Rea S, Goldsmith P, Cooper K B, Appleby R, Pardo D, Huggard P G, Krozer V, Shams H, Fice M, Renaud C, Seeds A, Stöhr A, Naftaly M, Ridler N, Clarke R, Cunningham J E, and Johnston M B 2017 *J. Phys. D: Appl. Phys.* **50** 043001
[7] Sengupta K, Nagatsuma T, and Mittleman D M 2018 *Nat. Electron.* **1** 622
[8] Jalas D, Petrov A, Eich M, Freude W, Fan S, Yu Z, Baets R, Popović M, Melloni A, Joannopoulos J D, Vanwolleghem M, Doerr C R, and Renner H 2013 *Nat. Photon.* **7** 579
[9] Shalaby M, Peccianti M, Ozturk Y, and Morandotti R 2013 *Nat. Commun.* **4** 1558
[10] Tamagnone M, Moldovan C, Poumirol J M, Kuzmenko A B, Ionescu A M, Mosig J R, and Perruisseau-Carrier J 2016 *Nat. Commun.* **7** 11216
[11] Mu Q, Fan F, Chen S, Xu S, Xiong C, Zhang X, Wang X, and Chang S 2019 *Photon. Res.* **7** 325
[12] Shuvaev A M, Astakhov G V, Pimenov A, Brüne C, Buhmann H, and Molenkamp L W 2011 *Phys. Rev. Lett.* **106** 107404
[13] Crassee I, Levallois J, Walter A L, Ostler M, Bostwick A, Rotenberg E, Seyller T, van der Marel D, and Kuzmenko A B 2011 *Nat. Phys.* **7** 48
[14] Shimano R, Yumoto G, Yoo J Y, Matsunaga R, Tanabe S, Hibino H, Morimoto T, and Aoki H 2013 *Nat. Commun.* **4** 1841
[15] Shalaby M, Peccianti M, Ozturk Y, Clerici M, Al-Naib I, Razzari L, Ozaki T, Mazhorova A, Skorobogatiy M, and Morandotti R 2012 *Appl. Phys. Lett.* **100** 241107
[16] Yuan S, Chen L, Wang Z, Deng W, Hou Z, Zhang C, Yu Y, Wu X, and Zhang X 2021 *Nat. Commun.* **12** 5570
[17] Zhao W Y, Zhao S H, Li H Y, Wang S, Wang S X, Utama M I B, Kahn S, Jiang Y, Xiao X, Yoo S, Watanabe K, Taniguchi T, Zettl A, and Wang F 2021 *Nature* **594** 517
[18] Nong J, Tang L, Lan G, Luo P, Guo C, Yi J, and Wei W 2020 *Nanophotonics* **9** 645
[19] Wang J, Song C, Hang J, Hu Z D, and Zhang F 2017 *Opt. Express* **25** 23880
[20] Fan Y, Shen N H, Zhang F, Wei Z, Li H, Zhao Q, Fu Q, Zhang P, Koschny T, and Soukoulis C M 2016 *Adv. Opt. Mater.* **4** 1824
[21] Zeng X, Fan L, and Zubairy M S 2017 *Phys. Rev. A* **95** 053850
[22] Low T and Avouris P 2014 *ACS Nano* **8** 1086
[23] Morgado T A and Silveirinha M G 2018 *ACS Photon.* **5** 4253
[24] Zhang Y, Zhou C L, Yi H L, and Tan H P 2020 *Phys. Rev. Appl.* **13** 034021
[25] Vaseashta A, Essaid M, Mustapha A, Didier M, and Amina F 2022 *Proc. Sixth Int. Symp. Dielectr. Mater. Appl.* (Springer Cham)
[26] Silalahi H M, Chen Y P, Shih Y H, Chen Y S, Lin X Y, Liu J H, and Huang C Y 2021 *Photon. Res.* **9** 1970
[27] Moon J Y, Kim M, Kim S I, Xu S, Choi J H, Whang D, Watanabe K, Taniguchi T, Park D S, Seo J, Cho S H, Son S K, and Lee J H 2020 *Sci. Adv.* **6** eabc6601